Optical Materials 120 (2021) 111408

Contents lists available at ScienceDirect

Optical Materials

journal homepage: www.elsevier.com/locate/optmat

Research Article

Solar driven photocatalytic degradation potential of novel graphitic carbon nitride based nano zero-valent iron doped bismuth ferrite ternary composite

Munib Ur Rahman [a], Umair Yaqub Qazi [b], Tajamal Hussain [c], Nimra Nadeem [a], Muhammad Zahid [a,*], Haq Nawaz Bhatti [a], Imran Shahid [d]

[a] Department of Chemistry, University of Agriculture, Faisalabad, Pakistan
[b] Department of Chemistry, College of Science University of Hafr Al Batin, P.O Box 1803, Hafr Al Batin 39524, Saudi Arabia
[c] Institute of Chemistry, University of Punjab Lahore, Pakistan
[d] Environmental Science Centre, Qatar University, Doha P.O. Box 2713, Qatar

ARTICLE INFO

Keywords:
Metal ferrite
Zero-valent iron
Response surface methodology
Ternary nanocomposites
Wastewater treatment

ABSTRACT

The synthetic industry has destroyed the life span of human beings due to environmental pollution. The discharged organic pollutants can be degraded by many physicochemical techniques, among them the heterogeneous photocatalysis is distinctive. Nano zero-valent iron (NZVI) doped bismuth ferrite ($BiFeO_3$) nanoparticles were composited with g-C_3N_4 to fabricate ternary NZVI@$BiFeO_3$/g-C_3N_4 semiconductor photocatalyst. The facile fabrication was achieved through the hydrothermal approach. The characterization techniques such as X-ray diffraction, Fourier transform infrared and Scanning electron microscopy equipped with energy dispersive X-ray was used. The analysis confirmed the successful fabrication of the photocatalysts. The energy bandgaps of the prepared photocatalysts were measured by the Tauc plot method using a UV–visible spectrophotometer. The energy bandgap values suggest that the insertion of g-C_3N_4 improves the optical response of catalysts under visible light. The NZVI@$BiFeO_3$/g-C_3N_4 was employed against Rhodamine B dye for photocatalytic oxidative degradation under sunlight radiations. The influencing parameters like pH, NZVI@$BiFeO_3$/g-C_3N_4 concentration, oxidant dose, reaction time were optimized to obtain the best-suited conditions. Under optimized conditions (i.e. pH = 9, NZVI@$BiFeO_3$/g-C_3N_4 = 10 mg/100 mL, oxidant = 18 mM, Time = 120 min) the g-C_3N_4 based composite photocatalyst showed ~97% oxidative degradation of Rhodamine B. Response surface methodology was used as a statistical tool to check the combinational effect of influencing parameters.

1. Introduction

Water is a precious natural resource and the gradual increase in the organic and inorganic contaminants in drinking water results in waterborne diseases. Over, one thousand million population in the world are consuming polluted water. Due to rapid development in industrialization and the use of pesticides, herbicides, and other chemicals -to improve yield in the agriculture sector-water pollution has become an unresolved global issue [1]. According to recent research, approximately 7 lac tons of organic synthetic dyes are producing worldwide per annum. Globally, about 28 lac tons/year of dyestuffs are ejected into the environment from various industrial sectors like leather goods, cosmetics, textile, hair color, paper, and food, etc. [2].

Conventionally, several wastewater treatment processes namely, membrane filtration, adsorption, and biodegradation are available for the degradation of contaminants in wastewater. Besides others, the advanced oxidation processes (AOPs) are among the most effective strategy for oxidative degradation of organic pollutants [3]. Among AOPs, heterogeneous photocatalysis (HPC) is a renewable, inexpensive, efficient, and easily deployed process. The AOPs can produce highly reactive oxygen species (ROS) like OH radicals for the non-selective degradation of several organic pollutants. The AOP dependent chemical reactions use chemical reactions and catalyzers for free radicle generation [4,5]. In photocatalysis, the light-mediated excitation of photocatalysts results in the redox reaction for the effective oxidation of pollutants. Numerous photocatalysts like, TiO_2, WO_3, $BiVO_4$, metal

* Corresponding author.
E-mail addresses: rmzahid@uaf.edu.pk, zahid595@gmail.com (M. Zahid).

https://doi.org/10.1016/j.optmat.2021.111408
Received 28 March 2021; Received in revised form 30 May 2021; Accepted 20 July 2021
Available online 26 July 2021

tungstate, and metal ferrites are available in the market as heterogeneous photocatalysts [6,7]. However, certain limitations of heterogeneous photocatalysis like low surface area, reduced photocatalytic activity, recombination of photogenerated charge carriers, as well as high cost may restrict their applications in wastewater [8].

Immobilization of metal-based photocatalysts over effective adsorbents may improve the application of these photocatalysts [9]. Besides other costly adsorbents like Graphene [6], CNTs, etc, graphitic carbon nitride (g-C_3N_4) is an effective adsorbent as well as photocatalyst. g-C_3N_4 has attained much attention due to its remarkable thermal and chemical stability, nontoxicity, narrow bandgap along, optical and electronic characteristics, unlike other carbon materials. It is an environmentally friendly metal-free photocatalyst and is highly used due to its low cost, polymeric p-conjugated structure [10]. The g-C_3N_4 structure is a heptazine ring type with an energy bandgap of ~2.8 eV. The efficient optical properties of g-C_3N_4 provide its potential application in improved photocatalysis under the visible region. Its structure resembles graphite and is a π conjugated polymer, but its layers possess strong C–N covalent bonds relative to the C–C bonds present in graphite [11]. The van der Waals forces are also present in its layers and it exhibits sunlight absorption in the range of 450 nm–460 nm. Its structure is undisturbed up to 600 °C while kept in the air [12]. g-C_3N_4 is used in photocatalysis, CO_2 reduction, degradation of organic contaminants, and hydrogen production by water splitting. Hassani and coworkers used $CoFe_2O_4$/mpg-C_3N_4 nanocomposite for the removal of acetaminophen (APAP) from aqueous solutions assisted with peroxymonosulfate activation [13]. The stable and recoverable composite provides 92% removal of APAP within 25 min without considerable leaching effect. The authors reported high efficiency of composite photocatalysts as compared to pristine metal oxides [13]. Different strategies for the improvement in the photocatalytic performance of metal oxide semiconductor has been developed, for example, surface incorporation of metal, non-metals, and semiconductor coupling [14]. Similarly, another study based on g-C_3N_4 reported the synthesis of mpg-C_3N_4/Ag/ZnO NWs/Zn plates using a facile dip-coating process for the effective degradation of direct orange 26 dye. The photocatalytic efficiency of 94% was achieved withing 120 min of reaction time using mpg-C_3N_4/Ag/ZnO NWs/Zn plates. The improved activity of the ZnO NWs/Zn plates was observed after the insertion of g-C_3N_4 [15].

Nano zero-valent iron-doped bismuth ferrite (NZVI@$BiFeO_3$) is a single-phase along with multiferroic material having simultaneous ferroelectric, ferromagnetic, as well as ferroelastic ordering. $BiFeO_3$ possesses potential applications in heterogeneous photocatalysis under the sunlight region [16]. Malathi and coworkers presented a comprehensive review on visible-light active Bi-based VO_4 photocatalyst [17]. Malathi and coworkers reported the use of $BiFeWO_6$/BiOI nanohybrid synthesized by wet impregnation method for photocatalytic and photoelectrochemical performance under visible light irradiations. The composite provides 92% degradation of RhB within 90 min of reaction time [18]. Similarly, $BiFeWO_6$/WO_3 nanocomposites were prepared by Priya and coworkers using a facile wet-chemical route. The tungsten-halogen lamp (250 W) was used as a light source for the photoexcitation of catalysts for RhB dye degradation. The composite showed 83% degradation of RhB in 60 min of reaction time [19].

This research work was aim at developing novel sunlight-driven ternary photocatalyst NZVI@$BiFeO_3$/g-C_3N_4 via the hydrothermal method and its implementation against Rhodamine B degradation. Doping of $BiFeO_3$ with nanoscale zero-valent iron and then composite with g-C_3N_4 was made to enhance the photocatalytic performance of photocatalyst. The characterization of the synthesized sample was carried out by using X-ray diffraction (XRD), Fourier Transform Infrared (FTIR) spectroscopy, Scanning Electron Microscopy- Energy dispersive X-ray (SEM-EDX). The UV–Vis spectrophotometer was also used to find the energy bandgap. The optimization of different parameters such as pH, catalyst dose, oxidant dose, and irradiation time was done. The fabrication of composite is done through the reaction of NZVI dope $BiFeO_3$ with g-C_3N_4, which resulted in increased absorption of sunlight radiations by the composite. The stability of composite photocatalyst was analyzed by determining the Fe leaching values of treated dye solution up to three reusability cycles by atomic absorption spectrophotometer (AAS). RSM was used for the optimization of influencing parameters of simulated dye wastewater using composites photocatalysts. RSM is a combination of statistical and mathematical techniques based on a multivariant non-linear model. It is used for experimental designing, mathematical model development, and optimization of independent to develop minimum or maximum response in the form of 3D surfaces [20].

2. Materials and methods

2.1. Chemicals

Analytical-grade chemicals were used in the synthesis process**.** Iron nitrate nonahydrate (Fe>98%), Bismuth nitrate pentahydrate (>98%), and Iron chloride (99%) were taken from Sigma Aldrich. Melamine (>98%), Rhodamine B (98%), and Ethanol (95.6%) were taken from DAEJUNG. Potassium hydroxide (98%), and Sodium borohydride (99%) were acquired from Sigma-Aldrich.

2.2. Synthesis

2.2.1. Synthesis of g-C_3N_4

g-C_3N_4 was fabricated via a simple pyrolysis method. 10g of melamine ($C_3H_6N_6$) in a ceramic crucible was directly placed in a muffle furnace at 550 °C. The heating rate was adjusted at 5 °C/min for 4 h. The yellow product was obtained after cooling at room temperature. The obtained product was converted into fine powered by grinding it in pestle and mortar for further use [21].

2.2.2. Synthesis of $BiFeO_3$

Bismuth ferrite nanoparticles were fabricated through the hydrothermal approach. A mixture with an equimolar concentration of Iron nitrate $Fe(NO_3)_3{\cdot}6H_2O$ and Bismuth nitrate $Bi(NO_3)_3{\cdot}5H_2O$ was made in 40 mL of 4 M Potassium hydroxide KOH, that used as a mineralizer. Now, the ultrasonication was carried out of the prepared solution for 15 min. Then, the solution was transferred into the 250 mL capacity Teflon-lined stainless-steel autoclave reactor for 6 h at 200 °C. After cooling, the $BiFeO_3$ nanoparticles were washed with water and 10% acetic acid to get pure $BiFeO_3$ nanoparticles. The product was dried out in a drying chamber at 90 °C in the air [22].

2.2.3. Synthesis of NZVI@$BiFeO_3$

The fabrication of NZVI@$BiFeO_3$ nanoparticles was done by implemented the reduction method. The 0.6 g ferric chloride ($FeCl_3{\cdot}6H_2O$) was taken and dissolved in 20 mL of ethanol. Eventually, 1.2 g of the $BiFeO_3$ material was added to the same solution. The temperature of the solution was maintained at 70 °C until the complete evaporation of ethanol. Now, the 0.6 g of $NaBH_4$ was added into 20 ml of distilled water and poured dropwise through the burette which resulted in the reduction of Fe^{3+} to Fe^0. The product was allowed to settle for 30 min. The magnetic solid nanoparticles were collected by applying an external magnetic field. The solid was washed with ethanol and distilled water until all the soluble salts were separated and then centrifuged. The drying of the sample was carried out in a vacuum chamber [23].

2.2.4. Synthesis of NZVI@$BiFeO_3$/g-C_3N_4 composite

The final composite was prepared by compositing the NZVI@$BiFeO_3$ with g-C_3N_4. In this reaction, the 0.2 g of NZVI@$BiFeO_3$ and 0.6 g of g-C_3N_4 were taken in 60 mL of distilled water. The mixture was ultrasonicated for 1 h. Now, the mixture was dried in the oven at 70 °C for 10 h. After the complete drying, the sample was carried out for calcination in the furnace at 200 °C for 2 h. The composite was converted into finely

divided powder using a pestle and mortar (Fig. 1) [24].

2.3. Characterization

The photocatalysts (g-C_3N_4 and $BiFeO_3$) and composite photocatalyst (NZVI@$BiFeO_3$/g-C_3N_4) were well characterized using XRD, FTIR, SEM, and UV visible spectroscopic techniques. The crystal phase analysis of catalysts was done using X-ray diffraction (Philips PANalytical Xpert pro DY 3805 powder XRD). The surface morphology and elemental composition were determined using scanning electron microscopy equipped with energy-dispersive X-ray (SEM–EDX; FEI NOVA 450 NANOSEM). The functional groups present on the surface of the prepared materials were determined using Fourier transformed infrared spectroscopy (Agilent Technology Cary 360 FTIR spectrophotometer). The optical response of $BiFeO_3$ and NZVI@$BiFeO_3$/g-C_3N_4 was check by calculating the bandgap energy (Tauc plot method) using a UV–visible spectrophotometer (CECIL CE-7200 UV visible spectrophotometer). Fe leaching test of treated RhB dye solution was performed using AAS (Hitachi Polarized Zeeman AAS, Z-8200, Japan) following the conditions described in AOAC (1990).

2.4. Photocatalytic degradation experiment

The oxidative photocatalytic degradation potential of the NZVI@-$BiFeO_3$/g-C_3N_4 composite was checked under ambient sunlight. The sunlight intensity was measure using a solar power meter (SM206) and brightness using a Lux meter.

The 100 mL of 10 ppm Rhodamine B solution was used for all experimental runs into 250 mL capacity borosilicate glass beakers. Typically, 10 mg NZVI@$BiFeO_3$/g-C_3N_4 was added into the 100 mL of dye solutions and the pH of solutions was maintained using 0.1 M NaOH and 0.1 M HCl solutions. After adjustment of solution pH, the beakers were kept in dark under constant stirring (160 rpm) on an orbital shaker for 30 min to attain the adsorption equilibrium of rhodamine B with the added composite. After 30 min, the adsorption was checked using a spectrophotometer. Afterward, oxidant was added, and solutions were placed under sunlight for oxidative photocatalysis. The average measured intensity of light was~ 1000 W/m^2 while the brightness was measured in the range of 88,000 ± 2000 Lux. The degradation reaction was carried out at midday when sky conditions were cleared. The samples were withdrawn after successive intervals centrifuged and absorbance was checked using a spectrophotometer at its λ_{max} = 554 nm. The % dye degradation was calculated using the formula given below:

$$\text{Degradation } (\%) = \left(\frac{A_o - A_t}{A_o}\right) \times 100 \quad (1)$$

Similarly, the effect of influencing experimental parameters i.e. pH, catalyst loading, oxidant dose, and reaction time was monitored using the process described above.

3. Results and discussion

3.1. Characterization

In the XRD pattern (shown in Fig. 2) of g-C_3N_4 and NZVI@$BiFeO_3$/g-C_3N_4, the strong characteristic peak at $2\theta = 27.04^\circ$ with the diffraction plane of (002) is attributed to the g-C_3N_4 [25]. However, in composite NZVI@$BiFeO_3$/g-C_3N_4 the peak with low intensity was observed because of the interaction among zero-valent iron-doped $BiFeO_3$ nanoparticles and g-C_3N_4. This lower intense peak relates to the interlayered stacked structure [1]. In the XRD pattern of $BiFeO_3$, the peaks corresponding to the characteristic XRD pattern of $BiFeO_3$ are present (JCPDS card no. 71–2494) [26]. The peak at $2\theta = 23.31^\circ$ with crystal plane

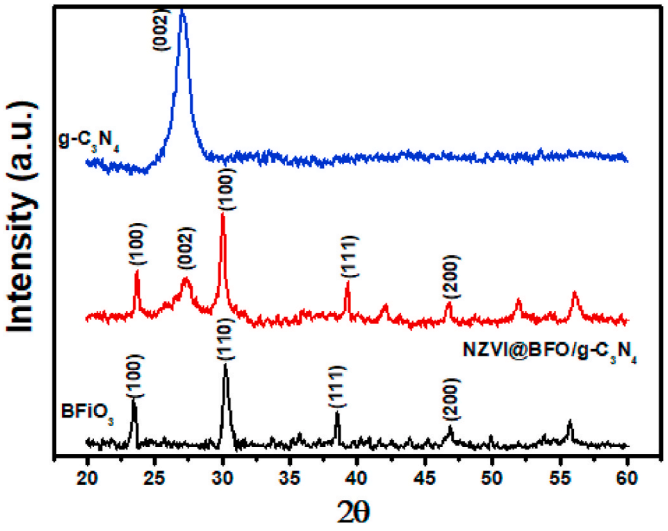

Fig. 2. XRD pattern of g-C_3N_4, $BiFeO_3$, and NZVI@$BiFeO_3$/g-C_3N_4

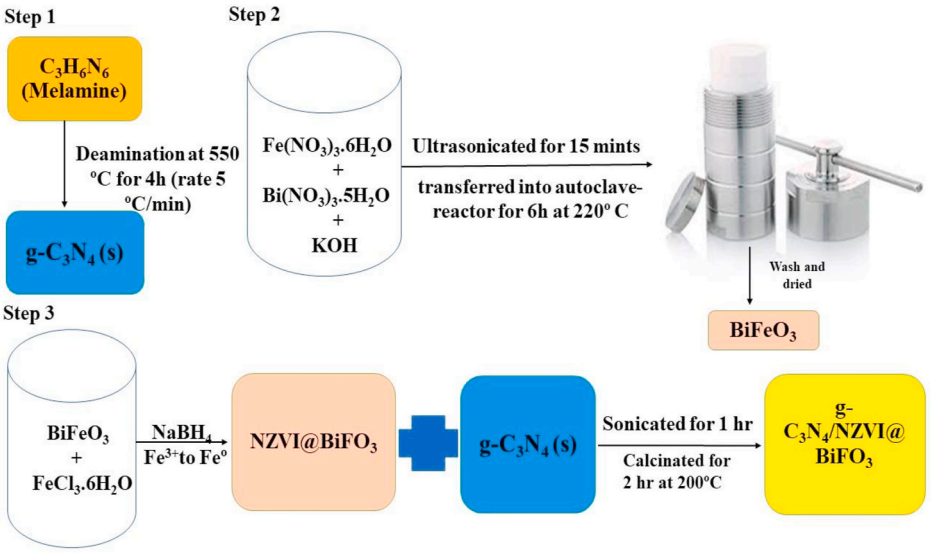

Fig. 1. A schematic representation for the synthesis of $BiFeO_3$ and NZVI@$BiFeO_3$/g-C_3N_4 composite.

(100) indicates the $BiFeO_3$ material also in the composite [17]. In the composite high intensity of peaks indicates the high crystallinity of prepared material [1]. The crystallite size was calculated using Sherer's formula (Eq (2)) [27];

$$D = \frac{K\lambda}{\beta Cos\theta} \quad (2)$$

Here, K indicates the Scherrer constant and its numerical value is 0.94 whereas, λ represents the wavelength of the X-ray source (i.e., 0.154 nm). D shows, crystallite size while β indicates the full width at half maximum of NZVI@$BiFeO_3$/g-C_3N_4 plane and Θ represents the diffraction angle. The value of crystallite size(D) for $BiFeO_3$ and NZVI@$BiFeO_3$/g-C_3N_4 was calculated as 59.99 nm and 21.58 nm respectively [28].

The FTIR results for prepared samples are presented in Fig. 3. The FTIR pattern of pristine g-C_3N_4 exhibits a strong peak in the range of 3000–3500 cm^{-1} which is attributed to the stretching vibrations of the N–H bond. Due to the presence of heterocycle belongs to the aromatic C–N stretching vibration peak are located at 1636 cm^{-1}, 1414 cm^{-1}, 1324 cm^{-1}, and 1240 cm^{-1}. The stretching vibration for the triazine unit is located at 810 cm^{-1} [29]. In the FTIR pattern of $BiFeO_3$, the large band at 3000–3600 cm^{-1} is due to the symmetric as well as antisymmetric stretching of H_2O and OH groups, and a band at 1630 cm^{-1} is related to the bending vibrations of H_2O. The band near 1384 cm^{-1} is owing to the existence of trapped nitrates. Moreover, the strong absorptive peaks at 400–600 cm^{-1} were attributed to the Fe–O stretching and bending vibration [22]. The NZVI@$BiFeO_3$/g-C_3N_4 composite possesses, all the characteristics peaks of g-C_3N_4 and $BiFeO_3$ while intensities in the composite are varied to some extent.

The SEM image (presented in Fig. 4) of composite (NZVI@$BiFeO_3$/g-C_3N_4) shows that NZVI@$BiFeO_3$ was layered on the g-C_3N_4 exterior in aggregate form. The composite processes rough surface due to the insertion of NZVI@$BiFeO_3$/g-C_3N_4 [30]. Fig. 4(a) indicates the typical layered and stacked structure of g-C_3N_4. The inset image in Fig. 4(a) represents the average size of g-C_3N_4 particles up to 500 nm [1].

The elemental composition of g-C_3N_4, $BiFeO_3$, and NZVI@$BiFeO_3$/g-C_3N_4 are presented in Fig. 5. The composite NZVI@$BiFeO_3$/g-C_3N_4 is composed of C, N, O, Fe, and Bi as shown in Fig. 5(c). The elemental mapping in Fig. 5(b) for $BiFeO_3$ depicts the existence of C, N, O, Na, K, iron, along with Bi. The elements other than O, Fe, and Bi are due to the other chemicals used in the protocol. The graphitic carbon nitride was made up of C, N and O confirmed by EDX elemental mapping.

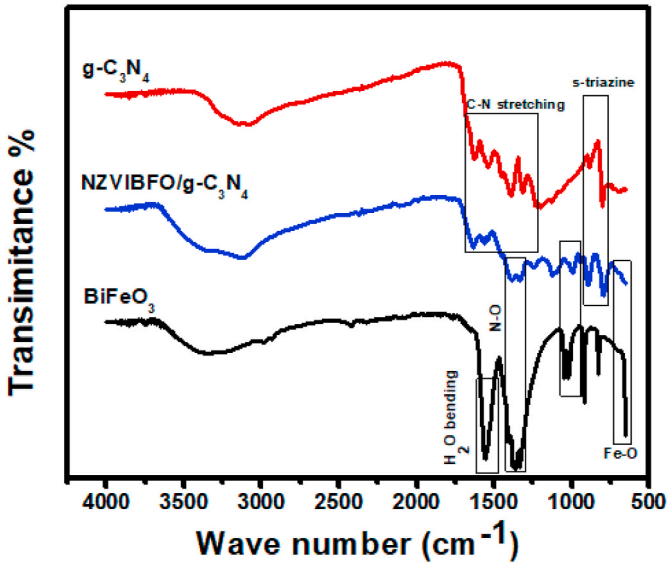

Fig. 3. FTIR analysis of g-C_3N_4, $BiFeO_3$, and NZVI@$BiFeO_3$/g-C_3N_4

To check out the optical properties of the prepared composite relative to the pure $BiFeO_3$, UV–Vis reflectance spectra are recorded of the synthesized samples. The absorbance wavelength of prepared samples lies in the Vis-region (400–800 nm) that confirmed the visible-light response capability of novel NZVI@$BiFeO_3$/g-C_3N_4 photocatalyst. For further study, the Tauc's equation employing the UV–vis absorption edges were used in the calculation of the bandgap energy of NZVI@$BiFeO_3$/g-C_3N_4 as shown in Eq (3).

$$(\alpha h\nu)^2 = K\ (h\nu\ -\ Eg) \quad (3)$$

Here, "**α**" is the absorption coefficient, "***h***" is Plank's constant, "***ν***" is the incident photon frequency, "**K**" is energy independent constant "$\mathbf{E_g}$" is energy bandgap energy, "**n**" is the nature of the transition in the semiconductor. The value of n is 2 for direct semiconductors. The bandgap was measured from the plot, $(\alpha h\nu)^2$ versus Energy (eV) [31]. The bandgap for pure $BiFeO_3$ as well as NZVI@$BiFeO_3$/g-C_3N_4 was 2.75 eV and 2.15 eV, respectively (Fig. 6). The presence of g-C_3N_4 in the composite narrowed the bandgap. This meant that the partition of photogenerated electrons-holes pairs (e^-/h^+) of NZVI@$BiFeO_3$/g-C_3N_4 would be better as well as effective in sunlight and resulting in enhancing photocatalytic performance. This might be due to the configuration of heterojunction against NZVI@$BiFeO_3$ as well as g-C_3N_4, which created interlacing frameworks of the valence band (VB) and the conducting band (CB) [32].

3.2. Impact of various parameters on photocatalytic activity

3.2.1. Effect of pH

The photocatalytic performance of the NZVI@$BiFeO_3$/g-C_3N_4 composite was analyzed at various pH values (2–11) and the results obtained after successive time intervals are presented in Fig. 7(a). It is clear from experimental results that under acid conditions the dye degradation was not very effective. With the gradual increase in pH values, the dye degradation also increases and reached the maximum at pH 9. The reason for high degradation at basic pH is due o the interaction of cationic dye Rhodamine B with the negative surface of the catalyst under basic solution pH. The negatively charged surface under basic conditions (i.e. pH = 9) promotes effective dye adsorption which results in improved dye degradation under sunlight. The lower degradation values under acidic conditions are due to the competition of cationic dye molecules with the H^+ ions present in the solution. Whereas, at pH above optimized i.e. 9, the degradation of RhB decreases gradually. The reason for this decrease in dye degradation under a high basic solution has been described by Refs. [31,33]. The scavenging of hydroxyl radicles under high basic conditions retard the dye degradation. Therefore, pH 9 was found most effective for Rhodamine B degradation using NZVI@-$BiFeO_3$/g-C_3N_4 with 120 min of reaction time [34].

3.2.2. Effect of catalyst concentration

The optimization of solid content is crucial for economic as well as for efficiency estimation of material. Therefore, the NZVI@$BiFeO_3$/g-C_3N_4 concentration was optimized by selecting the range of composite dose (2–18 mg) in 100 mL of Rhodamine B solution under optimized pH. The results of catalyst dose optimization are presented in Fig. 7(b). It can be seen from the results that by increasing the composite concentration, a gradual increase in dye degradation occurs which reached a maximum at 10 mg/100 mL of dye solutions. The increase in dye degradation with the increase in composite dose is due to the high adsorption capacity. The high adsorption of pollutant molecules promotes photocatalytic dye degradation. However, the further increase in solid content (i.e. above optimization) retard the dye degradation. The reason for this retarded degradation may be attributed to the overlapping of catalyst surface (making them less available for dye adsorption), and retardation in light penetration due to scattering of light at high catalyst concentration. Therefore, 10 mg/100 mL was found the optimize composite

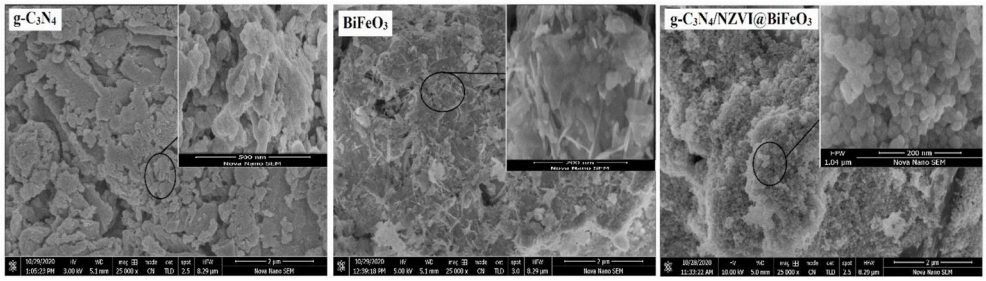

Fig. 4. SEM analysis of g-C_3N_4, $BiFeO_3$, and NZVI@$BiFeO_3$/g-C_3N_4

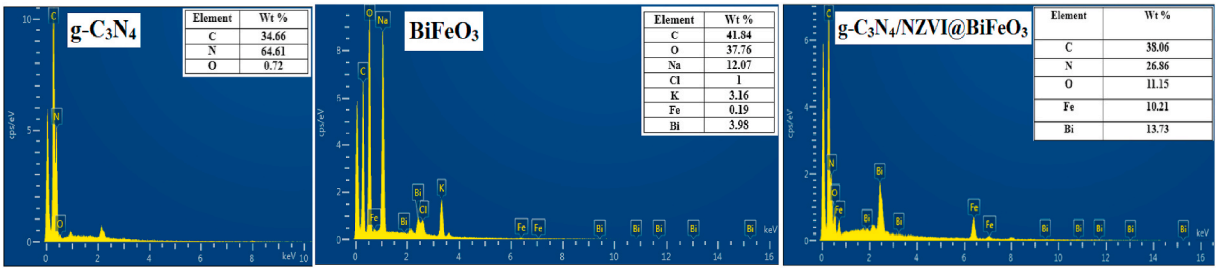

Fig. 5. EDX analysis of g-C_3N_4, $BiFeO_3$, and NZVI@$BiFeO_3$/g-C_3N_4

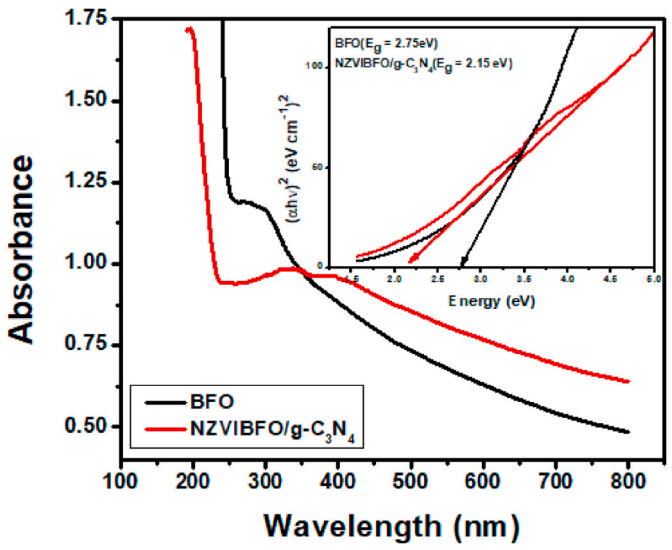

Fig. 6. UV–visible scans of $BiFeO_3$ and NZVI@$BiFeO_3$/g-C_3N_4, inset Tauc plot for energy bandgap.

concentration for effective dye degradation above which the balance between solid content and dye molecules disturbed [35].

3.2.3. Effect of oxidant dose

To explore the impact of oxidant dose on percentage degradation of RhB, the concentration of H_2O_2 was varied from 2 to 25 mM/100 ml of dye solution at optimized conditions of pH and composite dose. The results are presented in Fig. 7(c). A considerable increase in oxidative photocatalytic dye degradation was observed with the successive increase in hydrogen peroxide concentration. The working action of hydrogen peroxide follows a well-recognized reaction mechanism in the degradation of dye by the high rate of hydroxyl radical generation (Eq (4)). It also helps in charge separation by accepting the electron form conduction band (Eq (5)) [36]:

$$H_2O_2 + O_2^- \rightarrow HO^- + HO^{\cdot} + O_2 \quad (4)$$

$$H_2O_2 + e^-_{(CB)} \rightarrow HO^- + HO^{\cdot} \quad (5)$$

The result presents that 18 mM concentration of hydrogen peroxide was found optimized above which the further increase in oxidant concentration poses a negative impact on dye degradation [37,38]. Such effect results due to the hydrogen peroxide radical ($HO_2^{\cdot}$) formation. These are less reactive radicals than $HO^{\cdot}$ radicals and acts as $HO^{\cdot}$ scavengers according to Eq (6) and (7).

$$H_2O_2 + HO^{\cdot} \rightarrow H_2O + HO_2^{\cdot} \quad (6)$$

$$HO_2^{\cdot} + HO^{\cdot} \rightarrow H_2O + O_2 \quad (7)$$

3.2.4. Effect of irradiation time

For the optimization of reaction time, all three other parameters namely, pH, oxidant dose, and catalyst dose were kept constant at their optimized conditions while time was adjusted (10–160 min). The degradation of Rhodamine B was monitored by NZVI@$BiFeO_3$/g-C_3N_4 catalyst relative to the pristine $BiFeO_3$ after a successive interval of time. The absorbance was observed by spectrophotometer and represented in terms of percentage degradation in Fig. 7(d). It is obvious from the result that the percentage degradation was increased with the gradual increase in time by NZVI@$BiFeO_3$/g-C_3N_4 as well as pristine $BiFeO_3$ and reached a maximum at a certain limit. Above the maximum dye degradation further increase in reaction time does not improve the degradation process. NZVI@$BiFeO_3$/g-C_3N_4 catalyst degraded 97% of the dye after 120 min [39].

3.2.5. Stability/reusability test using NZVI@$BiFeO_3$/g-C_3N_4

The advantages of heterogeneous photocatalysts include their easy separation from the reaction mixture with remarkable activity after multiple reusability runs. To check the stability in terms of reusability of g-C_3N_4/NZVI@$BiFeO_4$ composite, the experiments were performed up to three successive runs. The composite was separated and washed with distilled water after every use dried and reweight. The results are presented in Fig. 8(a). The efficiency of composite decreases from ~97% to 94%, 87%, and 84% for 1st, 2nd, and 3rd reusability runs. The stable heterogeneous photocatalysts offer low leaching during phase change from solid to liquid media. Therefore, Fe leaching test was performed after each reusability run using AAS. The AAS analysis for Fe leaching

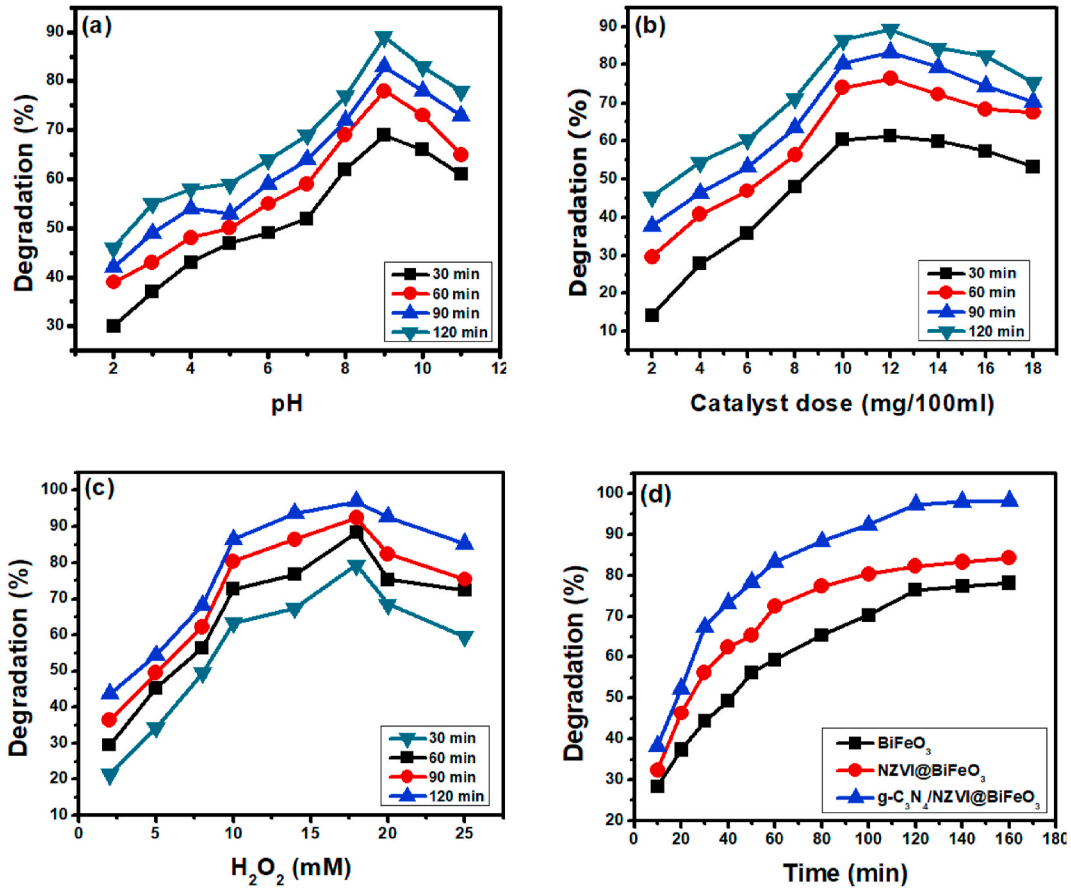

Fig. 7. Effect of different parameters on the degradation of Rhodamine B using NZVI@$BiFeO_3$/g-C_3N_4 (a) pH, (b) NZVI@$BiFeO_3$/g-C_3N_4 dose, (c) Oxidant conc., (d) reaction time at experimental conditions of pH = 9, NZVI@$BiFeO_3$/g-C_3N_4 = 10 mg/100 mL, H_2O_2 = 10 mM, time = 120 min, and ambient sunlight of ~1000 W/m^2 brightness = 88,000 ± 2000 LUX.

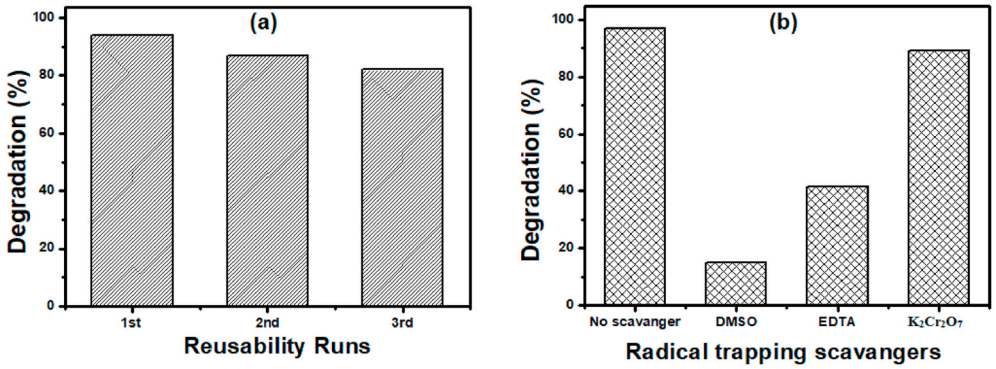

Fig. 8. (a) Stability analysis up to 3 reusability cycles and (b) radical trapping experiment using NZVI@$BiFeO_3$/g-C_3N_4

suggests good stability of composite after three runs (1.48 ppm, 0.42 ppm, and 0.27 ppm for 1st, 2nd, 3rd run respectively). The European Union Directives suggest that Fe values should not exceed 2 ppm [40]. In this study, the Fe leaching values are below the permissible limit provided by European Union Directives. Additionally, the small decrease in the efficiency of composite may be due to a decrease and/or blockage of the active site after multiple uses [9] (see Fig. 9).

3.2.6. *Radical trapping experiments using NZVI@$BiFeO_3$/g-C_3N_4*

Reactive species (i.e., OH radicals, h^+, and e^-) plays important role in the photocatalytic degradation process. Therefore, a radical scavenging test was performed to check the key radicals responsible for photocatalysis. For this, the 10 mM solutions of each scavenger i.e DMSO (dimethyl sulfoxide) for OH radical scavenging, EDTA (ethylene-diamine-tetra-acetate) for holes, and $K_2Cr_2O_7$ (potassium dichromate) for electron scavenging was used under the optimized conditions of pH, composite dose, oxidant dose, and reaction time [31]. The sunlight intensity recorded for scavenging experiments was ~1000 W/m^2 brightness = 94,000 ± 2000 LUX. The result obtained is presented in Fig. 8(b). It is obvious from the results that the addition of DMSO results reduction in degradation efficiency from ~97% to 15%. This means that OH radicals were the key agents for the photocatalytic degradation process. The addition of EDTA reduces the efficiency of the process from ~97% to 41.6% and $K_2Cr_2O_7$ reduces the process efficiency from ~97% to

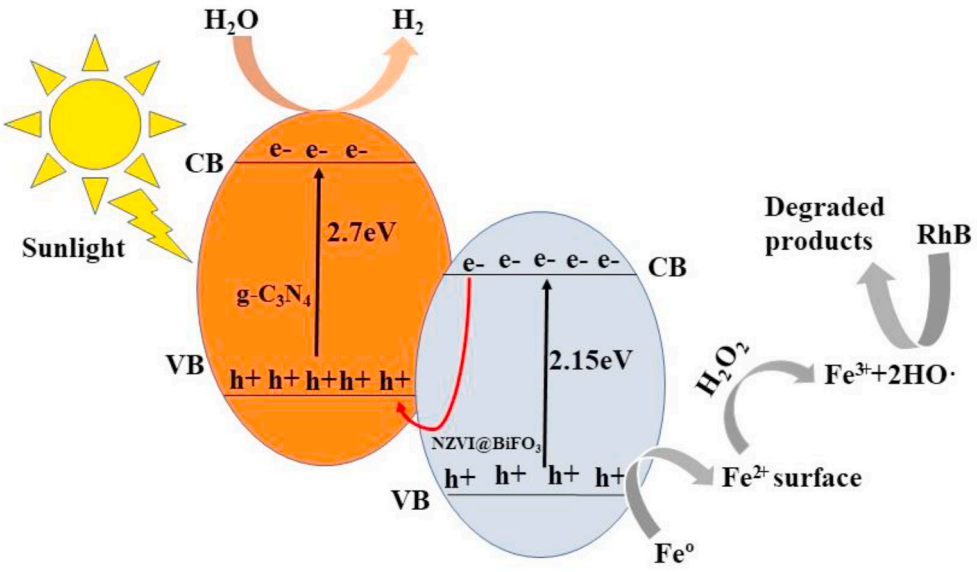

Fig. 9. Proposed photocatalytic degradation mechanism of RhB dye using NZVI@$BiFeO_3$/g-C_3N_4 composite.

89%. The results justify the effective contribution of holes and little contribution of electrons in the degradation process.

3.3Degradation mechanism

The proposed photocatalytic degradation mechanism offered by NZVI@$BiFeO_3$/g-C_3N_4 is as below; When the composite NZVI@$BiFeO_3$/g-C_3N_4 is excited under sunlight, the electrons-holes pairs (e^-/h^+) are created in both components (i.e. NZVI@$BiFeO_3$ and g-C_3N_4) due to their sunlight active behavior. The conduction band level of NZVI@$BiFeO_3$ is nearer to the valence band level of g-C_3N_4, therefor the photogenerated electrons (e^-) of NZVI@$BiFeO_3$ would be able to rejoin with photoinduced holes (h^+) of g-C_3N_4. At the same time, the excited electrons in the conduction band of g-C_3N_4 would participate in the reduction reactions to emit H_2. Concurrently, the photoproduced holes in the valance bands of NZVI@$BiFeO_3$ would participate in the oxidation of Rhodamine B dye. NZVI surface could produce at higher H_2O_2 concentration without the Fe^{2+} leaching. Consequently, the charge carrier's partition in the synthesized NZVI@$BiFeO_3$/g-C_3N_4 composite will enhance to a great extent. Hence, the composite processes strong oxidation as well reduction abilities respectively in the evolution of H_2 along with photodegradation of pollutants [41,42]. The overall proposed reaction mechanism for the Rhodamine B dye degradation is as follows.

$$g-C_3N_4/NZVI@BiFeO_3 + h\nu \rightarrow NZVI@BiFeO_3(e^- + h^+)/g - C_3N_4(e^- + h^+) \quad (8)$$

$$NZVI@BiFeO_3(e^- + h^+)/g - C_3N_4(e^- + h^+) \rightarrow NZVI@BiFeO_3(h^+)/g - C_3N_4(e^-) \quad (9)$$

$$g-C_3N_4(e^-) + 2\ H^+ \rightarrow H_2 \quad (10)$$

$$NZVI@BiFeO_3(h^+) + OH^- \rightarrow OH^{\cdot} \quad (11)$$

$$Fe^0 + 2H^+ \rightarrow Fe^{2+} + H_2 \quad (12)$$

$$Fe^{2+} + H_2O_2 \rightarrow Fe^{3+} + HO^- + HO^0 \quad (13)$$

$$Fe^{2+} - surface + H_2O_2 \rightarrow Fe^{3+} + 2OH^{\cdot} \quad (14)$$

$$OH^{\cdot} + RhB \rightarrow (Intermediates) \rightarrow Degraded\ products \quad (15)$$

The proposed sunlight active NZVI@$BiFeO_3$/g-C_3N_4 composite photocatalyst is a promising material as compared with previously reported $BiFeO_3$ composites. Previous research reported N-rGO supported Gd doped bismuth ferrite for photocatalytic degradation of RhB dye. The experiment was performed under Hg arc lamp and 99% degradation of RhB was achieved within 120 min of reaction time using 30 mg of composite in 250 mL dye solution. Similarly, Mn–Co doped Bismuth Ferrite/Ti_3C_2 MXene and Ag_3PO_4/$Bi_{25}FeO_{40}$/GO photocatalysts were studied under xenon lamps for CR and RhB dye degradation respectively (Table 1). The $BiFeO_3$/BiOI composite (75 mg/75 mL of RhB) was studied under a tungsten halogen lamp and ~100% degradation of RhB was achieved in 60 min of irradiation time [43–47]. Comparing the present novel composite with the prescribed material makes a good contribution in literature as no catalyst was studied under sunlight with such a small catalyst dose (Table 1).

3.4. Kinetics study

For the quantitative study of Rhodamine B degradation, reaction kinetics was analyzed by applying 1st as well as 2nd order reaction models to the experimental data. The expressions for the 1st and 2nd order kinetic models are presented in Eqs. (16) and (17) respectively [40].

$$\ln\ C_o / C_t = K_1 t \quad (16)$$

$$1/C_t - 1/C_o = K_2 t \quad (17)$$

Here, K_1 is the 1st order rate constant while C_0 and Ct are the concentrations of dye in solution at times zero and specific time t, respectively, and t is the reaction time [48]. K_1 and K_2 are the rates constant for the 1st and 2nd order kinetic model [49].

A linear relation between ln C_o/C_t and time is shown in Fig. 1**0(a)** and the value of k_1 is calculated to be the slope of a 1st order kinetics. Similarly, the value for K_2 is calculated from the plot ($1/C_t$-$1/C_o$) versus time as represented in Fig. 10(b). The R^2 value and rate constant k for RhB degradation are shown in Table 2. The R^2 value for 1st order kinetics is best fitted relative to the pseudo 2nd kinetics model [50] (see Table 3).

3.5. Optimization by response surface methodology for NZVI@$BiFeO_3$/g-C_3N_4

To observe photocatalytic degradation via statistical technique

Table 1
Comparative performance of previously reported $BiFeO_3$ based composites for organic pollutant removal.

Photocatalyst	Light source	Pollutant	Pollutant concentration	Other conditions	Irradiation time	PC efficiency	Ref.
N-rGO supported Gd doped bismuth ferrite	Hg arc lamp	RhB	10 ppm	30 mg/250 mL, unadjusted pH without oxidant	120	99%	[47]
Co-Doped Bismuth Ferrite	LED lamp (450–460 nm)	levofloxacin	15 ppm	0.5 g/L, pH = neutral, oxidant (PS) = 0.2 mM	60	~100%	[46]
$Ag_3PO_4/Bi_{25}FeO_{40}$/GO	Xenon lamp (35 W)	RhB	10 ppm	pH = unadjusted	75	96.9%	[45]
Mn-Codoped Bismuth Ferrite/Ti3C2 MXene	Xenon lamp (300 W),	Congo Red	100 ppm	100 mg/100 mL, unadjusted pH with no oxidant	30	93% in dark and 100% when irradiated	[44]
$BiFeO_3$/BiOI	Tungsten halogen lamp (250 W)	RhB	1×10^{-5} M	75 mg/75 mL, unadjusted pH without oxidant	60	~100%	[43]
NZVI@$BiFeO_3$/g-C_3N_4	Ambient sunlight	RhB	10 ppm	10 mg/100 mL, pH = 9, Oxidant = 18 mM	120	~97%	In this work

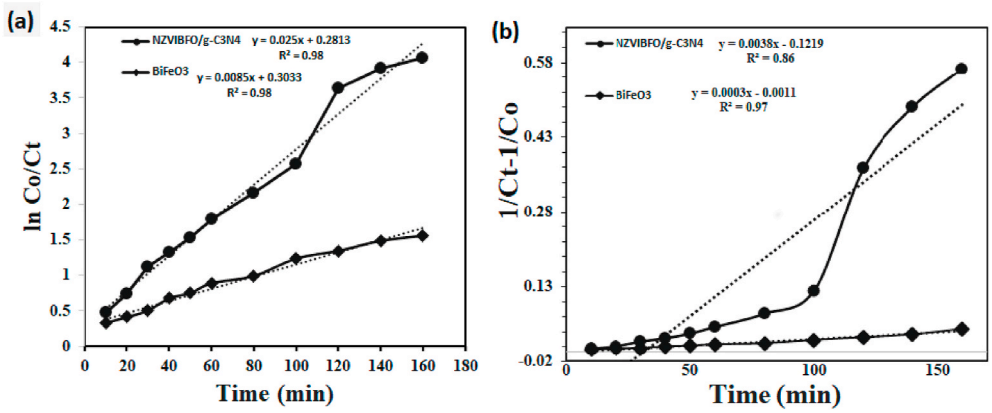

Fig. 10. Kinetic study (a) 1st order kinetic model (b) 2nd order kinetic model for Rhodamine B degradation using $BiFeO_3$ and NZVI@$BiFeO_3$/g-C_3N_4

Table 2
The calculated reaction rate constants of $BiFeO_3$ and NZVI@$BiFeO_3$/g-C_3N_4 towards photodegradation of RhB.

Catalysts	1st order kinetics		2nd order kinetics	
	R^2	K_1 (min^{-1})	R^2	K_2 (min^{-1})
$BiFeO_3$	0.9841	0.00833	0.9791	0.00014
NZVI@$BiFeO_3$/g-C_3N_4	0.9925	0.021	0.913	0.00096

response surface methodology (RSM) is a fascinating technique to optimize various factors [51]. Here, RSM under central composite design (CCD) was used to observe the impact of specific parameters on the photocatalytic degradation of Rhodamine B. The design was employed to attain the maximum response variable value (percentage degradation) by managing the independent variable such as pH, catalyst dose, and oxidant dose, under the visible light.

3.5.1. Analysis of variance (ANOVA)

It is obvious from the fitted summary plot that the significance of the model achieved is high. The prevailing condition of the significant model is the R^2 value that is almost equal to 1. However, there was a strong association observed between independent variables and dependent variables (i.e., percentage degradation) by the quadratic model. Additionally, to pose the significant influence on percentage degradation three factors pH, catalyst dose, and oxidant dose were monitored. The 2nd order polynomial equation was employed to define the response of three independent variables and their mutual relationship with the percentage degradation of Rhodamine B dye. According to the second-order polynomial model;

Table 3
ANOVA table for RhB degradation using NZVI@$BiFeO_3$/g-C_3N_4 composite.

Source	Sum of Squares	df	Mean Square	F Value	p-value Prob > F	
Model	13346.48	9	1482.94	38.18	<0.0001	Significant
A-pH	22.14	1	22.14	0.57	0.4676	
B-Catalyst dose	172.79	1	172.79	4.45	0.611	
C-Oxidant dose	115.87	1	115.87	2.98	0.1148	
AB	71.58	1	71.58	1.84	0.2044	
AC	101.03	1	101.03	2.60	0.1379	
BC	16.68	1	16.68	0.43	0.5271	
A^2	3620.98	1	3620.98	93.23	< 0.0001	
B^2	5426.29	1	5426.29	139.71	< 0.0001	
C^2	6286.44	1	6286.44	161.85	< 0.0001	
Residual	388.40	10	38.40			
Lack of Fit	322.14	5	64.43	4.86	0.0538	Not Significant
Pure Error	66.26	5	13.25			
Cor total	13734.88	19				

$$Y = \beta_0 + \sum_{i=1}^{k} \beta_i X_i + \sum_{i=1}^{k} \beta_{ii} X_i^2 + \sum_{i=1}^{k} \sum_{i \neq j}^{k} \beta_{ij} X_i X_j + \varepsilon \quad (18)$$

Here, Y indicates the response of dependent variable, βo represents the coefficient having a certain value while βi is related to linear coefficient, βii quadratic coefficient as well as βij shows the coefficient value of interaction effects. Xi and Xj indicate coded values for independent variables while ε represents the random error [7].

$$\%\ \text{Degradation of RhB} = +91.29 - 1.27 \times A + 3.56 \times B + 2.91 \times C + 2.99 \times A \times B - 3.55 \times A \times C + 1.44 \times B \times C - 15.85 \times A^2 - 19.40 \times B^2 - 20.89 \times C^2 \quad (19)$$

3.5.2. Optimization and combined effect of independent variables

The interaction effect of oxidant dose and catalyst dose was observed, and the results are represented in Fig. 11(a). Its contour, as well as 3D graph, indicated the maximum value for percentage degradation at optimized conditions. The catalyst dose was monitored in the range of 2–18 mg while the oxidant dose was maintained from 2 to 25 mM.

The results associated with the effect of pH and catalyst dose by RSM are shown in Fig. 11(b). The highest degradation value at optimized conditions (pH = 9 and catalyst dose 10mg/100 ml) is represented in the graph. Moreover, it may also be described that percentage degradation reached the maximum when the catalyst dose and pH increases. This is attributed to the increased surface area with increasing the catalyst dose. However, as the balance between the catalyst dose and pH condition is disturbed, a decrease in dye degradation was observed. The excess catalyst (i.e. above optimize) may cause the scattering of light radiations, results in the reduction of the percentage degradation. Eventually, there exists an interaction among excited and non-excited catalyst molecules which reduce the percentage degradation at excessive catalyst loading. On the other hand, the percentage degradation is almost diminished at the extreme value of catalyst dose and reduced pH.

The interactive results of pH and oxidant dose were observed productive on percentage degradation of RhB dye because the highest percentage degradation value was obtained by differing the pH 8 to 9 and increased oxidant dose Fig. 11(c). The degradation rate declines with more enhancement in oxidant dose due to the formation of H_2O_2 by recombination of the OH radicals. Therefore, at optimized pH = 9 along with optimized oxidant dose highest degree of percentage degradation was achieved [3].

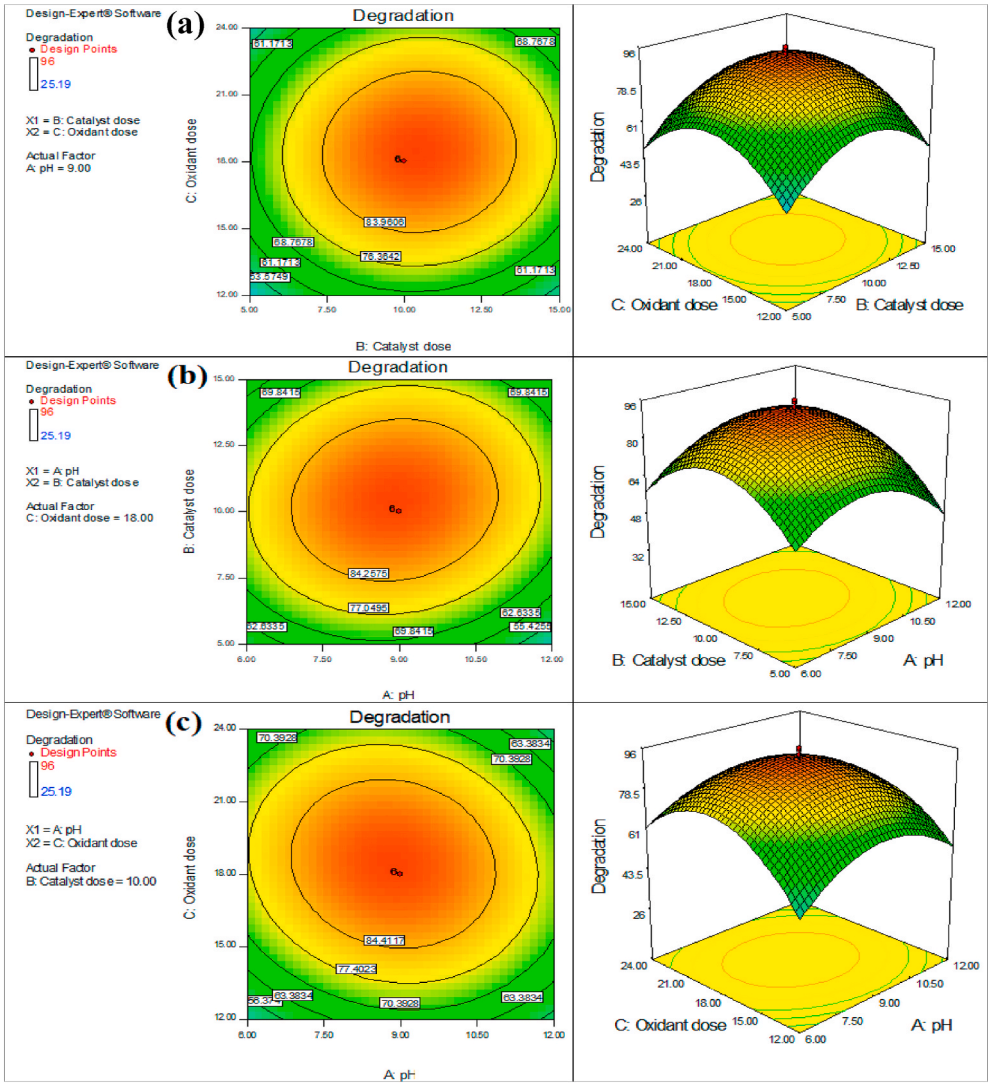

Fig. 11. Response Surface Methodology. L.H.S contour graph, R.H·S 3D graph (a) interaction of catalyst dose and oxidant dose (b) interaction of pH and catalyst dose (c) interaction of pH and oxidant dose.

4. Conclusion

The NZVI@$BiFeO_3$/g-C_3N_4 composite was synthesized through a hydrothermal route and applied to check out the photocatalytic degradation of Rhodamine B dye. The characterization analysis provides evidence for the successful synthesis of catalysts which also endorse the improved activity of composites having properties of both NZVI@$BiFeO_3$ and g-C_3N_4. The prepared composite degraded ~97% of Rhodamine B dye under solar light. The high optical response of NZVI@$BiFeO_3$/g-C_3N_4 under sunlight as compared to pristine $BiFeO_3$ is responsible for improved photocatalysis by the composite. The proposed mechanism for dye degradation describes that the composite provides efficient trapper sites for reactive species. Hence, the synthesized NZVI@$BiFeO_3$/g-C_3N_4 composite is a novel composite that would be applied in the future to oxidize several organic and inorganic contaminants from wastewater.

CRediT authorship contribution statement

Munib Ur Rahman: Data curation, Writing – original draft. **Umair Yaqub Qazi:** Methodology, Software. **Tajamal Hussain:** Conceptualization, Validation. **Nimra Nadeem:** Formal analysis, Writing – review & editing. **Muhammad Zahid:** Supervision, Project administration, Writing – review & editing. **Haq Nawaz Bhatti:** Resources, Investigation. **Imran Shahid:** Methodology, Revised draft preparation.

Declaration of competing interest

The authors declare that they have no known competing financial interests or personal relationships that could have appeared to influence the work reported in this paper.

Acknowledgments

Dr. Muhammad Zahid (corresponding author) is thankful to Higher Education Commission (HEC) Pakistan (Grant No.: 20-3898/NRPU/R&D/HEC/14/1019) for equipment and the University of Agriculture Faisalabad, Pakistan for facilities to conduct this research. The valuable support from Central Lab, LUMS Pakistan for the characterization of samples is highly acknowledged.

References

[1] R. Saher, M. Hanif, A. Mansha, H. Javed, M. Zahid, N. Nadeem, G. Mustafa, A. Shaheen, O. Riaz, Sunlight-driven photocatalytic degradation of rhodamine B dye by Ag/FeWO $_4$/gC $_3$ N $_4$ composites, Int. J. Environ. Sci. Tech. 18 (2021) 927–938.

[2] S.-M. Lam, J.-C. Sin, A.R. Mohamed, A review on photocatalytic application of g-C_3N_4/semiconductor (CNS) nanocomposites towards the erasure of dyeing wastewater, Mater. Sci. Semicond. Process. 47 (2016) 62–84.

[3] A. Tabasum, M. Zahid, H.N. Bhatti, M. Asghar, Fe_3O_4-GO composite as efficient heterogeneous photo-Fenton's catalyst to degrade pesticides, Mater. Res. Express 6 (2018), 015608.

[4] P. Yekan Motlagh, A. Khataee, T. Sadeghi Rad, A. Hassani, S.W. Joo, Fabrication of ZnFe-layered double hydroxides with graphene oxide for efficient visible light photocatalytic performance, J. Taiwan Inst. Chem. Eng. 101 (2019) 186–203.

[5] F. Ghanbari, F. Zirrahi, K.-Y.A. Lin, B. Kakavandi, A. Hassani, Enhanced electro-peroxone using ultrasound irradiation for the degradation of organic compounds: a comparative study, J. Environ. Chem. Eng. 8 (2020) 104167.

[6] M. Zahid, N. Nadeem, M.A. Hanif, I.A. Bhatti, H.N. Bhatti, G. Mustafa, Metal ferrites and their graphene-based nanocomposites: synthesis, characterization, and applications in wastewater treatment, in: K.A. Abd-Elsalam, M.A. Mohamed, R. Prasad (Eds.), Magnetic Nanostructures, Springer, Cham (Switzerland), 2019, pp. 181–212.

[7] K. Qureshi, M.Z. Ahmad, I.A. Bhatti, M. Zahid, J. Nisar, M. Iqbal, Graphene oxide decorated ZnWO4 architecture synthesis, characterization and photocatalytic activity evaluation, J. Mol. Liq. 285 (2019) 778–789.

[8] G. Iervolino, I. Zammit, V. Vaiano, L. Rizzo, Limitations and prospects for wastewater treatment by UV and visible-light-active heterogeneous photocatalysis: a critical review, Top. Curr. Chem. 378 (2020) 7.

[9] N. Nadeem, M. Zahid, Z. Rehan, M. Hanif, M. Yaseen, Improved photocatalytic degradation of dye using coal fly ash-based zinc ferrite (CFA/ZnFe $_2$ O $_4$) composite, Int. J. Environ. Sci. Tech. (2021) 1–16.

[10] H. Dong, X. Guo, C. Yang, Z. Ouyang, Synthesis of g-C_3N_4 by different precursors under burning explosion effect and its photocatalytic degradation for tylosin, Appl. Catal., B 230 (2018) 65–76.

[11] A. Thomas, A. Fischer, F. Goettmann, M. Antonietti, J.-O. Müller, R. Schlögl, J. M. Carlsson, Graphitic carbon nitride materials: variation of structure and morphology and their use as metal-free catalysts, J. Mater. Chem. 18 (2008) 4893–4908.

[12] J. Wen, J. Xie, X. Chen, X. Li, A review on g-C_3N_4-based photocatalysts, Appl. Surf. Sci. 391 (2017) 72–123.

[13] A. Hassani, P. Eghbali, B. Kakavandi, K.-Y.A. Lin, F. Ghanbari, Acetaminophen removal from aqueous solutions through peroxymonosulfate activation by $CoFe_2O_4$/mpg-C_3N_4 nanocomposite: insight into the performance and degradation kinetics, Environ. Technol. Innov. 20 (2020) 101127.

[14] C. Karthikeyan, P. Arunachalam, K. Ramachandran, A.M. Al-Mayouf, S. Karuppuchamy, Recent advances in semiconductor metal oxides with enhanced methods for solar photocatalytic applications, J. Alloys Compd. 828 (2020) 154281.

[15] A. Hassani, M. Faraji, P. Eghbali, Facile fabrication of mpg-C_3N_4/Ag/ZnO nanowires/Zn photocatalyst plates for photodegradation of dye pollutant, J. Photochem. Photobiol., A 400 (2020) 112665.

[16] S. Yang, G. Ma, L. Xu, C. Deng, X. Wang, Improved ferroelectric properties and band-gap tuning in BiFeO $_3$ films via substitution of Mn, RSC Adv. 9 (2019) 29238–29245.

[17] M. A, M. J, M. Ashokkumar, P. Arunachalam, A review on $BiVO_4$ photocatalyst: activity enhancement methods for solar photocatalytic applications, Appl. Catal., A 555 (2018) 47–74.

[18] A. Malathi, P. Arunachalam, A.N. Grace, J. Madhavan, A.M. Al-Mayouf, A robust visible-light driven $BiFeWO_6$/BiOI nanohybrid with efficient photocatalytic and photoelectrochemical performance, Appl. Surf. Sci. 412 (2017) 85–95.

[19] P. A, P. Arunachalam, S. A, M. J, A.M. Al-Mayouf, Synthesis of $BiFeWO_6$/WO_3 nanocomposite and its enhanced photocatalytic activity towards degradation of dye under irradiation of light, Colloids Surf., A 559 (2018) 83–91.

[20] A. Khataee, L. Alidokht, A. Hassani, S. Karaca, Response surface analysis of removal of a textile dye by a Turkish coal powder, Adv. Environ. Res. 2 (2013) 291–308.

[21] H. Sepahvand, S. Sharifnia, Photocatalytic overall water splitting by Z-scheme g-C_3N_4/$BiFeO_3$ heterojunction, Int. J. Hydrogen Energy 44 (2019) 23658–23668.

[22] C. Chen, J. Cheng, S. Yu, L. Che, Z. Meng, Hydrothermal synthesis of perovskite bismuth ferrite crystallites, J. Cryst. Growth 291 (2006) 135–139.

[23] E. Petala, M. Baikousi, M.A. Karakassides, G. Zoppellaro, J. Filip, J. Tuček, K. C. Vasilopoulos, J. Pechoušek, R. Zbořil, Synthesis, physical properties and application of the zero-valent iron/titanium dioxide heterocomposite having high activity for the sustainable photocatalytic removal of hexavalent chromium in water, Phys. Chem. Chem. Phys. 18 (2016) 10637–10646.

[24] Q. Wang, J. Tian, L. Wei, Y. Liu, C. Yang, Z-scheme heterostructure of Fe-doped SnO_2 decorated layered g-C_3N_4 with enhanced photocatalytic activity under simulated solar light irradiation, Opt. Mater. 101 (2020) 109769.

[25] M. Liu, Y. Jiao, J. Qin, Z. Li, J. Wang, Boron doped C_3N_4 nanodots/nonmetal element (S, P, F, Br) doped C_3N_4 nanosheets heterojunction with synergistic effect to boost the photocatalytic hydrogen production performance, Appl. Surf. Sci. 541 (2021) 148558.

[26] L. Di, H. Yang, T. Xian, J. Ma, H. Zhang, J. Jiang, Z. Wei, W. Feng, Growth of $BiFeO_3$ microcylinders under a hydrothermal condition, J. Nanomater. (2015) 175605.

[27] F. Mushtaq, M. Zahid, A. Mansha, I.A. Bhatti, G. Mustafa, S. Nasir, M. Yaseen, MnFe2O4/coal fly ash nanocomposite: a novel sunlight-active magnetic photocatalyst for dye degradation, Int. J. Environ. Sci. Tech. 17 (2020) 4233–4248.

[28] J. An, G. Zhang, R. Zheng, P. Wang, Removing lignin model pollutants with $BiFeO_3$–g-C_3N_4 compound as an efficient visible-light-heterogeneous Fenton-like catalyst, J. Environ. Sci. 48 (2016) 218–229.

[29] L. Zhang, Z. Jin, Y. Li, X. Hao, F. Han, Zn–Ni–P nanoparticles decorated gC $_3$ N $_4$ nanosheets applicated as photoanode in photovoltaic fuel cells, Catal. Lett. 149 (2019) 2397–2407.

[30] M.Y. Shami, M. Awan, M. Anis-ur-Rehman, Phase pure synthesis of $BiFeO_3$ nanopowders using diverse precursor via co-precipitation method, J. Alloys Compd. 509 (2011) 10139–10144.

[31] A. Tabasum, M. Alghuthaymi, U.Y. Qazi, I. Shahid, Q. Abbas, R. Javaid, N. Nadeem, M. Zahid, UV-accelerated photocatalytic degradation of pesticide over magnetite and cobalt ferrite decorated graphene oxide composite, Plants 10 (2021) 6.

[32] T. Wang, Y. Bai, W. Si, W. Mao, Y. Gao, S. Liu, Heterogeneous photo-Fenton system of novel ternary Bi_2WO_6/$BiFeO_3$/g-C_3N_4 heterojunctions for highly efficient degrading persistent organic pollutants in wastewater, J. Photochem. Photobiol., A 404 (2021) 112856.

[33] N. Nadeem, M. Zahid, A. Tabasum, A. Mansha, A. Jilani, I.A. Bhatti, H.N. Bhatti, Degradation of reactive dye using heterogeneous photo-Fenton catalysts: ZnFe2O4 and GO-ZnFe2O4 composite, Mater. Res. Express 7 (2020), 015519.

[34] E.T. Soares, M.A. Lansarin, C.C. Moro, A study of process variables for the photocatalytic degradation of rhodamine B, Braz. J. Chem. Eng. 24 (2007) 29–36.

[35] D. Shi, F. Yan, M. Wang, Y. Zou, T. Zheng, X. Zhou, L. Chen, Rhodamine derivative functionalized chitosan as efficient sensor and adsorbent for mercury (II) detection and removal, Mater. Res. Bull. 70 (2015) 958–964.

[36] W. Chu, W.K. Choy, T.Y. So, The effect of solution pH and peroxide in the TiO_2-induced photocatalysis of chlorinated aniline, J. Hazard Mater. 141 (2007) 86–91.

[37] A. Enesca, L. Isac, L. Andronic, D. Perniu, A. Duta, Tuning SnO_2–TiO_2 tandem systems for dyes mineralization, Appl. Catal., B 147 (2014) 175–184.

[38] M. Visa, C. Bogatu, A. Duta, Tungsten oxide – fly ash oxide composites in adsorption and photocatalysis, J. Hazard Mater. 289 (2015) 244–256.
[39] T.A. Saleh, V.K. Gupta, Functionalization of tungsten oxide into MWCNT and its application for sunlight-induced degradation of rhodamine B, J. Colloid Interface Sci. 362 (2011) 337–344.
[40] A. Tabasum, I.A. Bhatti, N. Nadeem, M. Zahid, Z.A. Rehan, T. Hussain, A. Jilani, Degradation of acetamiprid using graphene-oxide-based metal (Mn and Ni) ferrites as Fenton-like photocatalysts, Water Sci. Technol. 81 (2020) 178–189.
[41] S. Ali, M. Humayun, W. Pi, Y. Yuan, M. Wang, A. Khan, P. Yue, L. Shu, Z. Zheng, Q. Fu, Fabrication of $BiFeO_3$-g-C_3N_4-WO_3 Z-scheme heterojunction as highly efficient visible-light photocatalyst for water reduction and 2, 4-dichlorphenol degradation: insight mechanism, J. Hazard Mater. (2020) 122708.
[42] H.N. Bhatti, Z. Iram, M. Iqbal, J. Nisar, M. Khan, Facile synthesis of zero valent iron and photocatalytic application for the degradation of dyes, Mater. Res. Express 7 (2020), 015802.
[43] A. Malathi, P. Arunachalam, V.S. Kirankumar, J. Madhavan, A.M. Al-Mayouf, An efficient visible light driven bismuth ferrite incorporated bismuth oxyiodide ($BiFeO_3$/BiOI) composite photocatalytic material for degradation of pollutants, Opt. Mater. 84 (2018) 227–235.
[44] M.A. Iqbal, S.I. Ali, F. Amin, A. Tariq, M.Z. Iqbal, S. Rizwan, La- and Mn-codoped bismuth ferrite/Ti_3C_2 MXene composites for efficient photocatalytic degradation of Congo red dye, ACS Omega 4 (2019) 8661–8668.
[45] Y. Huang, X. Zhang, G. Zhu, Y. Gao, Q. Cheng, X. Cheng, Synthesis of silver phosphate/sillenite bismuth ferrite/graphene oxide nanocomposite and its enhanced visible light photocatalytic mechanism, Separ. Purif. Technol. 215 (2019) 490–499.
[46] X. Zhong, Z.-S. Zou, H.-L. Wang, W. Huang, B.-X. Zhou, Enhanced activation of persulfate by Co-doped bismuth ferrite nanocomposites for degradation of levofloxacin under visible light irradiation, Materials 12 (2019).
[47] T.K. Dixit, S. Sharma, A.S.K. Sinha, Synergistic effect of N-rGO supported Gd doped bismuth ferrite heterojunction on enhanced photocatalytic degradation of rhodamine B, Mater. Sci. Semicond. Process. 123 (2021) 105538.
[48] T. Fan, C. Chen, Z. Tang, Y. Ni, C. Lu, Synthesis and characterization of g-C_3N_4/$BiFeO_3$ composites with an enhanced visible light photocatalytic activity, Mater. Sci. Semicond. Process. 40 (2015) 439–445.
[49] Y.-S. Ho, Review of second-order models for adsorption systems, J. Hazard Mater. 136 (2006) 681–689.
[50] A. Tabasum, M. Alghuthaymi, U.Y. Qazi, I. Shahid, Q. Abbas, R. Javaid, N. Nadeem, M. Zahid, UV-accelerated photocatalytic degradation of pesticide over magnetite and cobalt ferrite decorated graphene oxide composite, Plants 10 (2021) 6.
[51] I.A. Bhatti, N. Ahmad, N. Iqbal, M. Zahid, M. Iqbal, Chromium adsorption using waste tire and conditions optimization by response surface methodology, J. Environ. Chem. Eng. 5 (2017) 2740–2751.